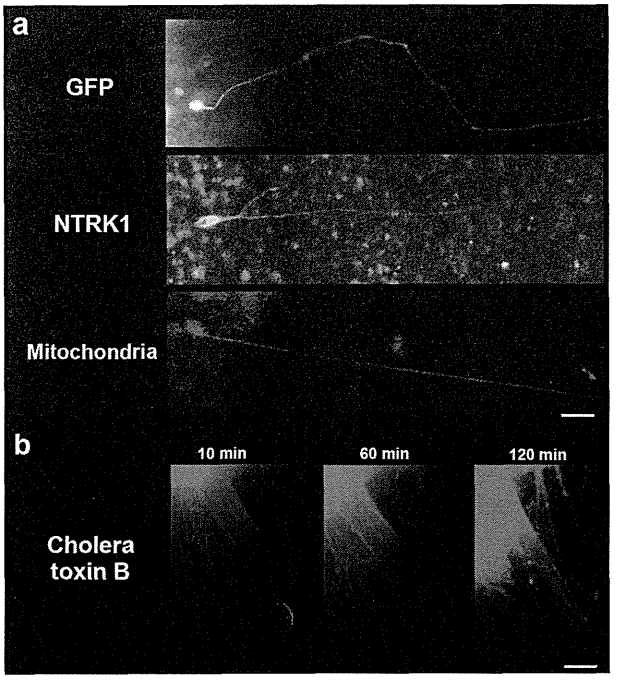

Figure 7 | Axonal transport in retinal ganglion cells. (a) Axonal transport was investigated for investigation of anterograde rapid flow employing NTRK1 and mitochondrial expression vectors. GFP was also used as a control. Plasmid vectors that carried each of these substances as well as the CMV promoter were directly introduced into the cell body using electroporation around D34. At approximately 7–10 h post-introduction, GFP expression was observed, which indicated that effective introduction of vectors by electroporation had been obtained. NTRK1 and mitochondria were identified in the cell body and in the axon, the latter location indicating anterograde rapid axonal transport. Scale bar, 80 μm. (b) A time series of axonal transport was also confirmed by the injection of Alexa-Fluo-555 conjugated cholera toxin B into retinal ganglion cell region. Cholera toxin was transported from the cell body to the peripheral area of axons by anterograde flow within approximately 2 h after injection. Scale bar, 100 μm.

systems, but without observation of the axons that would be expected with formation of the nerve fibre layers of the retina and the nerve fibre bundle of the optic nerve. In contrast, RGCs observed in the present study had long, prominent axons expressing NFs, Tuj1, and tau and growing in straight lines on the culture plate. The functionality of the axons was demonstrated by observation of axonal flow and action potentials. Anterograde axonal transport was identified by induction of both NTRK1- and mitochondria-specific vital stains and cholera toxin B into cell bodies. Sodium-dependent action potentials were demonstrated by patch clamp techniques.

RGCs were generated mostly in an OV-like clump of cells extruded from an EB where the layers of neural retina were supposed to differentiate. Most RGCs were localised to the marginal portion of the clump that adhered to the bottom of the culture dish. Because RGCs in vertebrates are located in the most anterior layer of the retina, which coincides with the marginal portion of the OV and optic cup in both embryogenesis and in previously established 3D culture systems, it is not surprising that our RGCs differentiated specifically at the surface of the clump, the inner portion of which may be an agglomerate of other retinal cell types. Relatively large cells with prominent nuclei, consistent with RGC morphology, were stratified at the marginal portion of the clump and were positive for Brn3b, the most specific marker for RGCs. Sectional analysis of RNA expression also confirmed that Brn3b expression was highest at the marginal portion of the clump without accompanying Crx expression, implying that the marginal portion of the clump had been specified purely into RGCs. This marginal portion, the RGCR, was able to survive for several weeks separated from the parent clump of cells (Fig. S3), suggesting the possibility of mechanically purifying RGCs for use in further investigations. Retinal cell determination progresses via a well-organised spatio-temporal pattern, in which RGCs appear initially and are followed by amacrine cells, photoreceptors, horizontal cells, bipolar cells, and Muller cells, a process that is highly conserved among species[47,66]In monkeys, RGC development begins around D25[67], and Brn3b, a characteristic transcriptional factor, is expressed in the retina of the human foetus at least by 8 weeks of gestation[68]. Thus, the timing of the marker expression and development of RGCs in our experiment resembles the process of the genesis of RGCs *in vivo*.

The axonal growth pattern differs significantly between 2D (on-dish) and 3D cultures. Two-dimensional culture methods for CNS neurons, including hippocampal[69], cortical[70,71], and hypothalamic cells[72,73], have been well established. These primary cultures can be augmented by coating the bottom of the culture dish with extracellular matrix components, including laminin, fibronectin, cadherin, and collagen, through which axons can extend[74]. In addition, neuroprotective agents, including BDNF[75,76], nerve growth factor[77], and CTNF[78,79], can easily be provided to the cells uniformly by adding them to the culture medium to further support neuron and axonal growth.

In contrast, the 3D culture approach has recently achieved *in vitro* organogenesis of CNS structures[80,81], including the retina[16,17,34], the pituitary gland[15] and heterogeneous neural tissue[82], in which axons generally extend into an extracellular matrix gel that contains collagen, fibronectin, or cadherin. Although 3D-cultured neurons seem more suitable for investigating stratified structures, branching, and synaptogenesis, the formation of long axons has not been obtained by previous 3D culture methods for retinogenesis. Achieving differentiation to normal RGCs by these methods may be too challenging because the surface of the self-induced retina directly contacts homogeneous culture fluid, which contains no extracellular matrix geometries capable of providing a foothold for horizontal extension of axons from RGCs. Expecting to achieve targeted horizontal extension of axons along the surface of the retina towards the optic nerve head, probably guided by extracellular signals such as Shh, BMP, and BDNF[83], would be even more difficult because self-induced retinas lack both the optic stalk and the nerve head.

Even in the environment of 2D culture where concentrations of multiple growth factors can be reliably controlled, neither self-induction of retinal layers nor prominent outgrowth of axons from RGCs have been achieved thus far. In the present study, axons extended from RGC bodies in response to a switch of the culture method from 3D to 2D at an optimal time, when the polarity and location of the new RGCs had just been determined. Supplementation with BDNF, a protective agent for RGCs, further supported axon growth. These spatio-temporal steps may be requirements for axon growth from RGCs. However, development of axons by a purely 3D culture method merits further research. RGC axons grown by the 3D to 2D culture method we established were formed uniformly, at a high rate, and in a short time and may contribute to various endeavours in basic and clinical science on human RGCs. For example, embryogenesis, nerve path finding, synaptogenesis, and interactions between nerve and glial cells in coculture may be easily investigated *in vitro*.

Our RGCs, which possessed long axons, also provided an excellent tool for investigating the pathogenesis and pathophysiology of optic nerve diseases. The optic nerve is composed of some 800,000–1,000,000 RGC axons[51] and can be anterogradely or retrogradely damaged by various crises, including ischemia, infection, trauma, inflammation, tumours, and genetic disorders. These can result in cell death and clinically severe visual impairment or blindness, such

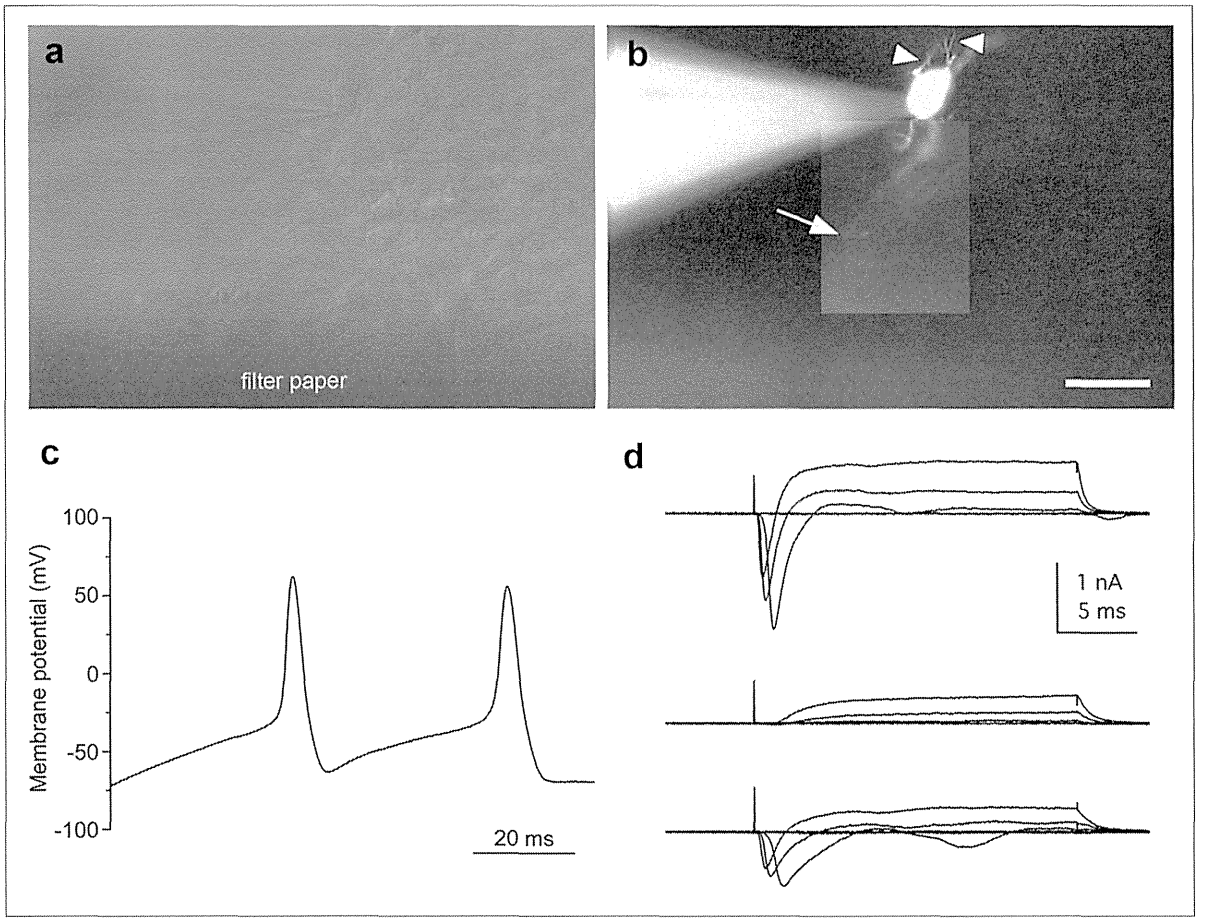

Figure 8 | Action potentials of the retinal ganglion cells. (a) Slice preparation of the cultured colony with recording electrode under DIC optics. (b) Composite photograph of an iPS cell-derived retinal ganglion cell filled with LY under fluorescence illumination. This cell exhibited some dendritic processes (arrowheads) and an axonal process (arrow). The same field is shown in (a) and (b). (c) Whole-cell recording of the retinal ganglion cells revealed action potentials in current-clamp mode (current injection of 60 pA). (d) A family of currents was recorded in voltage clamp mode in response to depolarising steps from a holding potential of −71 mV to target voltages increasing from −41 to +19 mV in 20-mV increments (upper traces). The fast inward currents were blocked by TTX (middle traces) and were recovered by washing (lower traces). Action potentials and inward currents were recorded from the LY-labelled cell shown in panel (b). Scale bar in panel (b), 30 μm.

as glaucoma. Glaucoma, a disease caused by high intraocular pressure, is an important cause of blindness globally. The pathogenesis and pathophysiology of many diseases associated with RGCs remain to be elucidated because of the difficulty of clinical examination of the deepest portions of the eyeball. RGCs induced by iPSCs derived from patients with RGC-associated diseases, especially genetic diseases, may further our understanding of the underlying molecular mechanisms of pathogenesis and pathophysiology. Precedents for this are already documented for other neurodegenerative diseases, including Parkinson' disease and Alzheimer's disease[84,85]. Moreover, the efficacy and toxicity of drugs for neuroprotection and support of axonal outgrowth and regeneration relevant to human RGC-associated diseases could be examined *in vitro* with our system with far more ease, accuracy, and safety than in the era of animal models. Indeed, an *in vitro* clinical study relevant to cardiac disease has already started[86,87]. In addition, future therapies involving isolation of human RGCs for transplantation to repair damaged optic nerves may benefit from our method, though several issues remain to be elucidated, including how to induce complex axonal projection patterns and synaptogenesis in the CNS target areas.

Methods

Ethical statement. The Ethics Committee of the National Institute for Child and Health Development (NCCHD) approved all experimental protocols (approval number #686, July 3, 2013). All experiments handling human cells and tissues were carried out in accordance with the Tenets of the Declaration of Helsinki.

Human iPSC culture. Human iPSCs (HPS0007_409B2 cell passage 29) were obtained from RIKEN BRC (Japan) and were maintained on a feeder layer of mouse embryonic fibroblasts (MEFs) inactivated by irradiation in Primate ES medium (ReproCELL) supplemented with 10 ng/mL recombinant human basic fibroblast growth factor (bFGF; Invitrogen, Carlsbad, CA, USA). For passaging, hiPSC colonies were detached and recovered from the feeder layer by treatment with dissociation solution (ReproCELL) at 37°C for 8 min. The detached hiPSC clumps were broken into smaller pieces consisting of several tens of cells by gentle pipetting. Cell passaging was performed at a 1 : 3 to 1 : 4 split ratio.

Induction of differentiation to RGCs. The induction of hiPSC differentiation employed a procedure based on SFEB methods[17]. hiPSCs were dissociated to single cells in TrypLE Express (Invitrogen) containing DNase I (0.05 mg/mL; Roche) and Y-27632 (10 μM; Wako) and were resuspended in retinal differentiation medium (RDM; G-MEM supplemented with 20% KSR, 0.1 mM nonessential amino acids, 1 mM pyruvate, 0.1 mM 2-mercaptoethanol, 100 U/mL penicillin, and 100 μg/mL streptomycin) containing Y-27636 and IWR-1e (20 and 3 μM, respectively; Merck Millipore). After separation from the feeder cells by decantation (the feeder cells adhered to the gelatine-coated bottom of the dish), the floating hiPSCs collected from the medium were seeded into V-bottomed low-cell-adhesion 96-well plates (Sumitomo Bakelite) at 9,000 cells per well. Matrigel (growth factor-reduced; BD Bioscience) was added to a final concentration of 0.5%–2% in the medium on day 2 (the day the suspension culture was initiated was defined as D0). On D12, the aggregates were transferred to low-cell-adhesion 24-well plates, and the medium was replaced with RDM containing Matrigel (0.5%–2%) and FBS (1%–10%). On D15, CHIR99021 (3 μM; Wako) and SAG (100 nM; Enzo Life Science) were added to the medium, and the suspension culture was continued for another 3 days. On D18, the

aggregates were transferred to retinal maturation medium (RMM; DMEM/F12-Glutamax medium containing the N2 supplement, 100 U/mL penicillin, and 100 μg/mL streptomycin) and were then cultured in the absence of FBS. The adhesion culture started when the aggregates were transferred to poly-D-lysine/laminin-coated 24-well plates (BD Bioscience) in RMN medium containing FBS and 100 ng/mL BDNF (R&D Systems). The start day varied from D26 to D29, and the addition of retinoic acid (0.5 μM; Sigma) 3 days prior to the start of adhesion culture was preferred. The concentration of FBS was increased stepwise from 1% up to 10% over the course of the adhesion culture.

Real-time reverse transcription polymerase chain reaction (RT-PCR). Total RNA was extracted from cells using an RNeasy Mini Kit (QIAGEN, Valencia, CA, USA). The expression levels of the mRNAs in each RNA sample were determined using the StepONE Sequence Detection System (Applied Biosystems). RT-PCR was performed using a One Step SYBR PrimeScript PLUS RT-PCR Kit (TaKaRa Bio, Shiga, Japan). The primers used in this study are listed in Supplementary Table 1. The thermocycler conditions were as follows: an initial hold at 42°C for 5 min; incubation at 95°C for 10 s; and then 40 cycles at 95°C for 5 s and 60°C for 31 s. The expression of mRNA was assessed by evaluating threshold cycle (C_T) values. The C_T values were normalised to the expression level of hypoxanthine phosphoribosyltransferase 1 (HPRT1), and the relative amount of mRNA specific to each of the target genes was calculated using the $2^{-\Delta\Delta CT}$ method.

To perform sectional gene expression analysis, adherent tissues of EBs and extruding OVs were defined as three parts: the RGCR, which was located at the outermost 2–3 layers of cells in the clump of cells; the OVR, which was an adherent structure of OVs excluding the RGCR; and the MBEB, which was an adherent structure of the EB. The regions were obviously identified under a SZ61 stereomicroscope (Olympus), and mechanical separation using a 25-G needle was performed under the same microscope.

Frozen section preparation. Specimens were fixed in 4% paraformaldehyde in 100 mM phosphate buffer for 3 h at 4°C, then rinsed in phosphate buffer, osmotic pressure-conditioned in a graded series of sucrose solutions in phosphate buffer up to 30%, and embedded in OCT compound (Tissue-Tek; Sakura Finetek). Each block was serially sectioned at 5-μm thickness using a CryoStar NX70 (Thermo Fisher Scientific).

Immunohistochemistry. Immunostaining was performed using frozen sections or whole cells fixed on the dish. Whole cells specimens were fixed with 4% paraformaldehyde (pH 7.0) for 20 min at room temperature. After two rinses with PBS, specimens were incubated with 0.1% Triton X-100 for 15 min at room temperature and then washed three times with PBS for 5 min each. Specimens of frozen sections or whole cells were then incubated with 3% bovine serum albumin (BSA) for 30 min at room temperature followed by primary antibody incubation for 16 h at 4°C. The primary antibodies used in this study and their dilutions are listed in Supplementary Table 2. Secondary antibody reactions were carried out by incubation with the corresponding species-specific Alexa Fluor-488-conjugated antibodies (1 : 500, Invitrogen) for 1 h at room temperature in the dark. After four washes with PBS for 5 min each, specimens were mounted with ProLong Gold Antifade Reagent with DAPI (Invitrogen) and viewed with an IX71 inverted research microscope (Olympus) or BZ-9000E (KEYENCE).

Haematoxylin and eosin staining. Specimens were fixed in 4% paraformaldehyde in 100 mM phosphate buffer for 3 h at 4°C, rinsed in water, dehydrated in a graded series of alcohols/xylene, and embedded in paraffin. Each block was serially sectioned at a 3-μm thickness. Deparaffinized sections were then stained with haematoxylin and eosin.

Transmission electron microscopy. Specimens were fixed in 2% glutaraldehyde in 100 mM cacodylate buffer for 2 h, followed by 1% osmium tetroxide in 100 mM cacodylate buffer for 1 h. Specimens were then dehydrated in a graded series of alcohols/xylene, permeated with propylene oxide, and embedded in epoxy resin. Ultrathin sections of representative areas were stained with uranyl acetate and lead citrate and viewed with a JEM-1200EX electron microscope (Japan Electron Optics Laboratory).

Axonal flow observation. The NTRK1 expression vector (RG213091; ORIGENE), the pPAmCherry-Mito Vector (TaKaRa Bio), and the pcDNA™6.2/C-EmGFP Vector (Invitrogen) were electroporated into cultured cells. For electroporation, NEPA21 (NEPAGENE) with platinum electrodes was used. The cultured colony was injected with fast green-dyed DNA solution using a sharp glass pipette, placed between the electrodes, and electroporated with voltage pulses (poring pulse: voltage 100 V, width 2.5 ms, interval 50 ms, two times; transfer pulse: voltage 20 V, width 50 ms, interval 50 ms, five times). The cultured cells were then allowed to develop in humidified incubators. Observations were made with an IX71 inverted research microscope (Olympus).

The time series of anterograde axonal flow was conducted by injection of Alexa Fluo-555 conjugated cholera toxin subunit B (Life Technologies) into the RGCR. Time-lapse analysis was performed immediately after the injection of cholera toxin B with a DeltaVision ELITE (CORNES Technologies).

Electrophysiological recordings. Colonies were cultured on mixed cellulose ester filter papers (0.2-μm pore size; ADVANTEC) for 1 week. After removal of filter paper bearing colonies from the medium, suction was applied to the bottom of the filter to cause the colonies to attach firmly. Slices 200 μm thick were then cut vertically with a custom-made tissue chopper and fixed to the glass bottom of a recording chamber having a volume of 1.5 mL with a small amount of silicone grease (Dow Corning). All experiments were performed at physiological temperatures (35–37°C) using a ThermoClamp-1 (Automate Scientific). The chamber was continuously perfused at 1.5 mL/min with extracellular solution containing 120 mM NaCl, 3 mM KCl, 2.5 mM $CaCl_2$, 1 mM $MgCl_2$, 10 mM glucose, and 25 mM $NaHCO_3$ equilibrated with 95%/5% O_2/CO_2 (pH 7.4). Chemicals were purchased from Sigma unless otherwise noted. Whole-cell patch-clamp recordings were made from the retinal ganglion cells located on the outer perimeter of the cultured colony. Recordings were performed with an Axopatch 200B amplifier (Molecular Devices) using pCLAMP 9.2 software (Molecular Devices). The slice preparations were visualised using an upright microscope (BX50WI; Olympus) equipped with DIC optics and a 60× water-immersion objective. The voltage or current trace was low-pass filtered (Bessel filter, corner frequency 10 kHz) and sampled at 20–50 kHz with a Digidata 1322A interface (Molecular Devices). Voltage-dependent Na^+ currents were measured with leakage and capacitive current subtraction (P/-5 protocol) and were averaged over three trials. In some experiments, we added 1 μM tetrodotoxin (TTX) to the extracellular solution to block voltage-dependent Na^+ channels. The recording pipettes (6–8 MΩ) were filled with an intracellular solution containing 120 mM K gluconate, 6 mM KCl, 2 mM NaCl, 1 mM $CaCl_2$, 1 mM $MgCl_2$, 5 mM EGTA, 10 mM HEPES, 4 mM Na_2ATP, and 0.5 mM GTP (pH 7.2). In all experiments, Lucifer Yellow CH dilithium salt (LY; 0.05%) was added to the intracellular solutions to visualise the morphology of the recorded cells. Liquid junction potentials (−11 mV) were corrected. The average series resistance (Rs) was 29.4 ± 4.77 MΩ (n = 5). Rs was compensated by 40%. Data with Rs values of more than 35 MΩ were excluded from the analyses. The average membrane capacitance during the recordings was 7.20 ± 2.84 pF (n = 5). Current and voltage data were acquired using pCLAMP 9.2 software and saved on a custom-built personal computer (Physio-Tech). Analyses were performed with Clampfit 9.2 (Molecular Devices) and OriginPro 8J (OriginLab). Images of LY-filled cells were captured using a high-gain colour camera (HCC-600; Flovel) and saved using INFO.TV Plus software (Infocity). The images were adjusted for brightness and contrast and complemented by pasting in a part of another image obtained from a different depth of the slice preparation using Photoshop CS6 software (Adobe Systems). All data are presented as means ± SDs.

1. Pascolini, D. & Mariotti, S. P. Global estimates of visual impairment: 2010. *Br. J. Ophthalmol.* **96**, 614–618 (2012).
2. Resnikoff, S. *et al.* Global data on visual impairment in the year 2002. *Bull. World Health Organ.* **82**, 844–851 (2004).
3. Rattner, A. & Nathans, J. Macular degeneration: recent advances and therapeutic opportunities. *Nat. Rev. Neurosci.* **7**, 860–872 (2006).
4. Hartong, D. T., Berson, E. L. & Dryja, T. P. Retinitis pigmentosa. *Lancet* **368**, 1795–1809 (2006).
5. Quigley, H. A. & Broman, A. T. The number of people with glaucoma worldwide in 2010 and 2020. *Br. J. Ophthalmol.* **90**, 262–267 (2006).
6. Sun, G., Asami, M., Ohta, H., Kosaka, J. & Kosaka, M. Retinal stem/progenitor properties of iris pigment epithelial cells. *Dev. Biol.* **289**, 243–252 (2006).
7. Haruta, M. *et al.* Induction of photoreceptor-specific phenotypes in adult mammalian iris tissue. *Nat. Neurosci.* **4**, 1163–1164 (2001).
8. Tropepe, V. *et al.* Retinal stem cells in the adult mammalian eye. *Science* **287**, 2032–2036 (2000).
9. Osakada, F. *et al.* Wnt signaling promotes regeneration in the retina of adult mammals. *J. Neurosci.* **27**, 4210–4219 (2007).
10. Lawrence, J. M. *et al.* MIO-M1 cells and similar muller glial cell lines derived from adult human retina exhibit neural stem cell characteristics. *Stem Cells* **25**, 2033–2043 (2007).
11. Seko, Y. *et al.* Derivation of human differential photoreceptor-like cells from the iris by defined combinations of CRX, RX and NEUROD. *PLoS One* **7**, e35611 (2012).
12. Lamba, D. A. *et al.* Generation, purification and transplantation of photoreceptors derived from human induced pluripotent stem cells. *PLoS One* **5**, e8763 (2010).
13. Jayaram, H. *et al.* Transplantation of photoreceptors derived from human Muller glia restore rod function in the P23H rat. *Stem Cells Transl. Med.* **3**, 323–333 (2014).
14. Eiraku, M. *et al.* Self-organized formation of polarized cortical tissues from ESCs and its active manipulation by extrinsic signals. *Cell Stem Cell* **3**, 519–532 (2008).
15. Suga, H. *et al.* Self-formation of functional adenohypophysis in three-dimensional culture. *Nature* **480**, 57–62 (2011).
16. Eiraku, M. *et al.* Self-organizing optic-cup morphogenesis in three-dimensional culture. *Nature* **472**, 51–56 (2011).
17. Nakano, T. *et al.* Self-formation of optic cups and storable stratified neural retina from human ESCs. *Cell Stem Cell* **10**, 771–785 (2012).
18. Assawachananont, J. *et al.* Transplantation of embryonic and induced pluripotent stem cell-derived 3D retinal sheets into retinal degenerative mice. *Stem Cell Rep.* **2**, 662–674 (2014).

19. Meyer, J. S. *et al.* Modeling early retinal development with human embryonic and induced pluripotent stem cells. *Proc. Natl. Acad. Sci. U. S. A.* **106**, 16698–16703 (2009).
20. Meyer, J. S. *et al.* Optic vesicle-like structures derived from human pluripotent stem cells facilitate a customized approach to retinal disease treatment. *Stem Cells* **29**, 1206–1218 (2011).
21. Zhong, X. *et al.* Generation of three-dimensional retinal tissue with functional photoreceptors from human iPSCs. *Nat. Commun.* **5**, 4047 (2014).
22. Ikeda, H. *et al.* Generation of Rx+/Pax6+ neural retinal precursors from embryonic stem cells. *Proc. Natl. Acad. Sci. U. S. A.* **102**, 11331–11336 (2005).
23. Osakada, F. *et al.* Toward the generation of rod and cone photoreceptors from mouse, monkey and human embryonic stem cells. *Nat. Biotechnol.* **26**, 215–224 (2008).
24. Lamba, D. A., Karl, M. O., Ware, C. B. & Reh, T. A. Efficient generation of retinal progenitor cells from human embryonic stem cells. *Proc. Natl. Acad. Sci. U. S. A.* **103**, 12769–12774 (2006).
25. Hirami, Y. *et al.* Generation of retinal cells from mouse and human induced pluripotent stem cells. *Neurosci. Lett.* **458**, 126–131 (2009).
26. Mellough, C. B., Sernagor, E., Moreno-Gimeno, I., Steel, D. H. & Lako, M. Efficient stage-specific differentiation of human pluripotent stem cells toward retinal photoreceptor cells. *Stem Cells* **30**, 673–686 (2012).
27. Yu, D. Y. *et al.* Retinal ganglion cells: Energetics, compartmentation, axonal transport, cytoskeletons and vulnerability. *Prog. Retin. Eye Res.* **36**, 217–246 (2013).
28. Kaplan, E. & Benardete, E. The dynamics of primate retinal ganglion cells. *Prog. Brain Res.* **134**, 17–34 (2001).
29. Hong, S., Iizuka, Y., Kim, C. Y. & Seong, G. J. Isolation of primary mouse retinal ganglion cells using immunopanning-magnetic separation. *Mol. Vis.* **18**, 2922–2930 (2012).
30. Zhang, X. M. *et al.* Immunopanning purification and long-term culture of human retinal ganglion cells. *Mol. Vis.* **16**, 2867–2872 (2010).
31. Takihara, Y. *et al.* Dynamic imaging of axonal transport in living retinal ganglion cells in vitro. *Invest. Ophthalmol. Vis. Sci.* **52**, 3039–3045 (2011).
32. Xie, B. B. *et al.* Differentiation of retinal ganglion cells and photoreceptor precursors from mouse induced pluripotent stem cells carrying an atoh7/math5 lineage reporter. *PLoS One* **9**, e112175 (2014).
33. Riazifar, H., Jia, Y., Chen, J., Lynch, G. & Huang, T. Chemically induced specification of retinal ganglion cells from human embryonic and induced pluripotent stem cells. *Stem Cells Transl. Med.* **3**, 424–432 (2014).
34. Gonzalez-Cordero, A. *et al.* Photoreceptor precursors derived from three-dimensional embryonic stem cell cultures integrate and mature within adult degenerate retina. *Nat. Biotechnol.* **31**, 741–747 (2013).
35. Zuber, M. E., Gestri, G., Viczian, A. S., Barsacchi, G. & Harris, W. A. Specification of the vertebrate eye by a network of eye field transcription factors. *Development* **130**, 5155–5167 (2003).
36. Bailey, T. J. *et al.* Regulation of vertebrate eye development by Rx genes. *Int. J. Dev. Biol.* **48**, 761–770 (2004).
37. Riesenberg, A. N. *et al.* Pax6 regulation of Math5 during mouse retinal neurogenesis. *Genesis* **47**, 175–187 (2009).
38. Brown, N. L., Patel, S., Brzezinski, J. & Glaser, T. Math5 is required for retinal ganglion cell and optic nerve formation. *Development* **128**, 2497–2508 (2001).
39. Wang, S. W. *et al.* Requirement for math5 in the development of retinal ganglion cells. *Genes Dev.* **15**, 24–29 (2001).
40. Ghiasvand, N. M. *et al.* Deletion of a remote enhancer near ATOH7 disrupts retinal neurogenesis, causing NCRNA disease. *Nat. Neurosci.* **14**, 578–586 (2011).
41. Hutcheson, D. A. & Vetter, M. L. The bHLH factors Xath5 and XNeuroD can upregulate the expression of XBrn3d, a POU-homeodomain transcription factor. *Dev. Biol.* **232**, 327–338 (2001).
42. Qiu, F., Jiang, H. & Xiang, M. A comprehensive negative regulatory program controlled by Brn3b to ensure ganglion cell specification from multipotential retinal precursors. *J. Neurosci.* **28**, 3392–3403 (2008).
43. Pan, L., Deng, M., Xie, X. & Gan, L. ISL1 and BRN3B co-regulate the differentiation of murine retinal ganglion cells. *Development* **135**, 1981–1990 (2008).
44. Green, E. S., Stubbs, J. L. & Levine, E. M. Genetic rescue of cell number in a mouse model of microphthalmia: interactions between Chx10 and G1-phase cell cycle regulators. *Development* **130**, 539–552 (2003).
45. Furukawa, T., Morrow, E. M. & Cepko, C. L. Crx, a novel otx-like homeobox gene, shows photoreceptor-specific expression and regulates photoreceptor differentiation. *Cell* **91**, 531–541 (1997).
46. Chen, S. *et al.* Crx, a novel Otx-like paired-homeodomain protein, binds to and transactivates photoreceptor cell-specific genes. *Neuron* **19**, 1017–1030 (1997).
47. Cepko, C. L., Austin, C. P., Yang, X., Alexiades, M. & Ezzeddine, D. Cell fate determination in the vertebrate retina. *Proc. Natl. Acad. Sci. U. S. A.* **93**, 589–595 (1996).
48. Tagaya, M. *et al.* Syntaxin 1 (HPC-1) is associated with chromaffin granules. *J. Biol. Chem.* **270**, 15930–15933 (1995).
49. Bennett, M. K., Calakos, N. & Scheller, R. H. Syntaxin: a synaptic protein implicated in docking of synaptic vesicles at presynaptic active zones. *Science* **257**, 255–259 (1992).
50. Tsukiji, N. *et al.* Mitf functions as an in ovo regulator for cell differentiation and proliferation during development of the chick RPE. *Dev Biol* **326**, 335–346 (2009).
51. Hogan, M. J., Alvarado, J. A. & Weddel, J. E. Histology of the Human Eye: An Atlas and Textbook. 537 (1971).
52. Drager, U. C. & Olsen, J. F. Ganglion cell distribution in the retina of the mouse. *Invest. Ophthalmol. Vis. Sci.* **20**, 285–293 (1981).
53. Stone, J., Makarov, F. & Hollander, H. The glial ensheathment of the soma and axon hillock of retinal ganglion cells. *Vis. Neurosci.* **12**, 273–279 (1995).
54. Wollner, D. A. & Catterall, W. A. Localization of sodium channels in axon hillocks and initial segments of retinal ganglion cells. *Proc. Natl. Acad. Sci. U. S. A.* **83**, 8424–8428 (1986).
55. Ninkina, N. *et al.* Gamma-synucleinopathy: neurodegeneration associated with overexpression of the mouse protein. *Hum. Mol. Genet.* **18**, 1779–1794 (2009).
56. Balaratnasingam, C., Morgan, W. H., Johnstone, V., Cringle, S. J. & Yu, D. Y. Heterogeneous distribution of axonal cytoskeleton proteins in the human optic nerve. *Invest. Ophthalmol. Vis. Sci.* **50**, 2824–2838 (2009).
57. Goedert, M. & Spillantini, M. G. A century of Alzheimer's disease. *Science* **314**, 777–781 (2006).
58. Bull, N. D., Guidi, A., Goedert, M., Martin, K. R. & Spillantini, M. G. Reduced axonal transport and increased excitotoxic retinal ganglion cell degeneration in mice transgenic for human mutant P301S tau. *PLoS One* **7**, e34724 (2012).
59. Yuan, A. *et al.* Alpha-internexin is structurally and functionally associated with the neurofilament triplet proteins in the mature CNS. *J. Neurosci.* **26**, 10006–10019 (2006).
60. Yuan, A., Rao, M. V., Veeranna & Nixon, R. A. Neurofilaments at a glance. *J. Cell Sci.* **125**, 3257–3263 (2012).
61. Bates, C. A. & Meyer, R. L. The heavy neurofilament protein is expressed in regenerating adult but not embryonic mammalian optic fibers in vitro. *Exp. Neurol.* **119**, 249–257 (1993).
62. Cui, Q., Tang, L. S., Hu, B., So, K. F. & Yip, H. K. Expression of trkA, trkB, and trkC in injured and regenerating retinal ganglion cells of adult rats. *Invest. Ophthalmol. Vis. Sci.* **43**, 1954–1964 (2002).
63. Klein, R., Jing, S. Q., Nanduri, V., O'Rourke, E. & Barbacid, M. The trk proto-oncogene encodes a receptor for nerve growth factor. *Cell* **65**, 189–197 (1991).
64. Vossel, K. A. *et al.* Tau reduction prevents Abeta-induced defects in axonal transport. *Science* **330**, 198 (2010).
65. Phillips, M. J. *et al.* Blood-derived human iPS cells generate optic vesicle-like structures with the capacity to form retinal laminae and develop synapses. *Invest. Ophthalmol. Vis. Sci.* **53**, 2007–2019 (2012).
66. Livesey, F. J. & Cepko, C. L. Vertebrate neural cell-fate determination: lessons from the retina. *Nat. Rev. Neurosci.* **2**, 109–118 (2001).
67. Rapaport, D. H., Rakic, P. & LaVail, M. M. Spatiotemporal gradients of cell genesis in the primate retina. *Perspect. Dev. Neurobiol.* **3**, 147–159 (1996).
68. Pacal, M. & Bremner, R. Induction of the ganglion cell differentiation program in human retinal progenitors before cell cycle exit. *Dev. Dyn.* **243**, 712–729 (2014).
69. Ray, J., Peterson, D. A., Schinstine, M. & Gage, F. H. Proliferation, differentiation, and long-term culture of primary hippocampal neurons. *Proc. Natl. Acad. Sci. U. S. A.* **90**, 3602–3606 (1993).
70. Lesuisse, C. & Martin, L. J. Long-term culture of mouse cortical neurons as a model for neuronal development, aging, and death. *J. Neurobiol.* **51**, 9–23 (2002).
71. Sciarretta, C. & Minichiello, L. The preparation of primary cortical neuron cultures and a practical application using immunofluorescent cytochemistry. *Methods Mol. Biol.* **633**, 221–231 (2010).
72. Guerra-Crespo, M., Ubieta, R., Joseph-Bravo, P., Charli, J. L. & Perez-Martinez, L. BDNF increases the early expression of TRH mRNA in fetal TrkB+ hypothalamic neurons in primary culture. *Eur. J. Neurosci.* **14**, 483–494 (2001).
73. Joseph-Bravo, P., Perez-Martinez, L., Lezama, L., Morales-Chapa, C. & Charli, J. L. An improved method for the expression of TRH in serum-supplemented primary cultures of fetal hypothalamic cells. *Brain Res. Brain Res. Protoc.* **9**, 93–104 (2002).
74. Barros, C. S., Franco, S. J. & Muller, U. Extracellular matrix: functions in the nervous system. *Cold Spring Harb. Perspect. Biol.* **3**, a005108 (2011).
75. Almeida, R. D. *et al.* Neuroprotection by BDNF against glutamate-induced apoptotic cell death is mediated by ERK and PI3-kinase pathways. *Cell Death Differ.* **12**, 1329–1343 (2005).
76. Melo, C. V. *et al.* Spatiotemporal resolution of BDNF neuroprotection against glutamate excitotoxicity in cultured hippocampal neurons. *Neuroscience* **237**, 66–86 (2013).
77. Sofroniew, M. V., Howe, C. L. & Mobley, W. C. Nerve growth factor signaling, neuroprotection, and neural repair. *Annu. Rev. Neurosci.* **24**, 1217–1281 (2001).
78. Sendtner, M., Kreutzberg, G. W. & Thoenen, H. Ciliary neurotrophic factor prevents the degeneration of motor neurons after axotomy. *Nature* **345**, 440–441 (1990).
79. Peterson, W. M., Wang, Q., Tzekova, R. & Wiegand, S. J. Ciliary neurotrophic factor and stress stimuli activate the Jak-STAT pathway in retinal neurons and glia. *J. Neurosci.* **20**, 4081–4090 (2000).
80. Kadoshima, T. *et al.* Self-organization of axial polarity, inside-out layer pattern, and species-specific progenitor dynamics in human ES cell-derived neocortex. *Proc. Natl. Acad. Sci. U. S. A.* **110**, 20284–20289 (2013).
81. Lancaster, M. A. *et al.* Cerebral organoids model human brain development and microcephaly. *Nature* **501**, 373–379 (2013).
82. Kato-Negishi, M., Morimoto, Y., Onoe, H. & Takeuchi, S. Millimeter-sized neural building blocks for 3D heterogeneous neural network assembly. *Adv. Healthc. Mater.* **2**, 1564–1570 (2013).

83. Lowery, L. A. & Van Vactor, D. The trip of the tip: understanding the growth cone machinery. *Nat. Rev. Mol. Cell Biol.* **10**, 332–343 (2009).
84. Chung, C. Y. *et al.* Identification and rescue of alpha-synuclein toxicity in Parkinson patient-derived neurons. *Science* **342**, 983–987 (2013).
85. Kondo, T. *et al.* Modeling Alzheimer's disease with iPSCs reveals stress phenotypes associated with intracellular Abeta and differential drug responsiveness. *Cell Stem Cell* **12**, 487–496 (2013).
86. Dimos, J. T. *et al.* Induced pluripotent stem cells generated from patients with ALS can be differentiated into motor neurons. *Science* **321**, 1218–1221 (2008).
87. Yazawa, M. *et al.* Using induced pluripotent stem cells to investigate cardiac phenotypes in Timothy syndrome. *Nature* **471**, 230–234 (2011).

Acknowledgments

We thank Dr H. Akutsu for technical instruction on primary culture of iPSCs. This work was supported by a Grant from the Ministry of Health, Labour, and Welfare (H24-Nanchi-Ippan-031), JSPS KAKENHI (grant numbers 22390327 and 24659770) and a grant from the National Centre for Child Health and Development 25-7.

Author contributions

T.T. and T.Y. performed experiments, analysed and interpreted data, and wrote the manuscript. F.T. and S.W. designed and performed the electrophysiological recordings and contributed to the writing of the manuscripts. S.N. interpreted data. N.A. designed experiments and supervised the project.

Additional information

Supplementary information accompanies this paper at http://www.nature.com/scientificreports

Competing financial interests: The authors declare no competing financial interests.

How to cite this article: Tanaka, T. *et al.* Generation of retinal ganglion cells with functional axons from human induced pluripotent stem cells. *Sci. Rep.* **5**, 8344; DOI:10.1038/srep08344 (2015).

PLOS | ONE

RESEARCH ARTICLE

Morphological Features and Important Parameters of Large Optic Discs for Diagnosing Glaucoma

Satoshi Okimoto[1]*, **Keiko Yamashita**[2], **Tetsuo Shibata**[2], **Yoshiaki Kiuchi**[1]

1 Department of Ophthalmology and Visual science, Graduate School of Biomedical Sciences, Hiroshima University, Hiroshima, Japan, 2 Shibata Eye Clinic, Hyogo, Japan

* okimoto@hiroshima-u.ac.jp

Citation: Okimoto S, Yamashita K, Shibata T, Kiuchi Y (2015) Morphological Features and Important Parameters of Large Optic Discs for Diagnosing Glaucoma. PLoS ONE 10(3): e0118920. doi:10.1371/journal.pone.0118920

Academic Editor: Sanjoy Bhattacharya, Bascom Palmer Eye Institute, University of Miami School of Medicine;, UNITED STATES

Received: June 16, 2014

Accepted: January 7, 2015

Published: March 23, 2015

Data Availability Statement: All relevant data are within the paper and its Supporting Information files.

Funding: Shibata Eye Clinic provided support in the form of salaries for authors KY and TS, but did not have any additional role in the study design, data collection and analysis, decision to publish, or preparation of the manuscript. The specific roles of these authors are articulated in the "author contributions" section.

Competing Interests: KY and TS are employees of Shibata Eye Clinic. There are no patents, products in

Abstract

Purpose

To compare the optic disc parameters of glaucomatous eyes to those of non-glaucomatous eyes with large discs.

Methods

We studied 225 consecutive eyes with large optic discs (>2.82 mm2): 91 eyes with glaucoma and 134 eyes without glaucoma. An eye was diagnosed with glaucoma when visual field defects were detected by the Humphrey Field Analyzer. All of the Heidelberg Retina Tomograph II (HRT II) parameters were compared between the non-glaucomatous and glaucomatous eyes. A logistic regression analysis of the HRT II parameters was used to establish a new formula for diagnosing glaucoma, and the sensitivity and specificity of the Moorfields Regression Analysis (MRA) was compared to the findings made by our analyses.

Results

The mean disc area was 3.44±0.50 mm2 in the non-glaucomatous group and 3.40±0.52 mm2 in the glaucoma group. The cup area, cup volume, cup-to-disc area ratio, linear cup/disc ratio, mean cup depth, and the maximum cup depth were significantly larger in glaucomatous eyes than in the non-glaucomatous eyes. The rim area, rim volume, cup shape measurement, mean retinal nerve fiber layer (RNFL) thickness, and RFNL cross-sectional area were significantly smaller in glaucomatous eyes than in non-glaucomatous eyes. The cup-to-disc area ratio, the height variation contour (HVC), and the RNFL cross-sectional area were important parameters for diagnosing the early stage glaucoma, and the cup-to-disc area ratio and cup volume were useful for diagnosing advanced stage glaucoma in eyes with a large optic disc. The new formula had higher sensitivity and specificity for diagnosing glaucoma than MRA.

development, or marketed products to declare. This does not alter our adherence to all the PLOS ONE policies on sharing data and materials.

Conclusions

The cup-to-disc area ratio, HVC, RNFL cross-sectional area, and cup volume were important parameters for diagnosing glaucoma in eyes with a large optic disc. The important disc parameters to diagnose glaucoma depend on the stage of glaucoma in patients with large discs.

Introduction

Glaucoma is a progressive optic neuropathy in which morphological changes of the optic disc and the retinal nerve fiber layer (RNFL) progress to visual field defects [1,2]. Because the rim area of the optic disc is reduced in glaucomatous eyes, evaluating the changes of the optic disc morphology is essential for diagnosing glaucoma [3–7]. In general, the optic disc cup area is increased in glaucomatous eyes, and the cup-to-disc ratio is used for diagnosing glaucoma [8]. However, the cup area is also large in eyes with a large optic disc, and these eyes may not be glaucomatous [9,10]. Therefore, a careful examination is needed to discriminate whether a large cup area is due to glaucoma or to a large optic disc.

The Heidelberg Retina Tomograph II (HRT II; Heidelberg Engineering, GmbH, Heidelberg, Germany) can obtain highly reproducible measurements of the stereometric parameters of the optic disc, and these parameters can be used to differentiate normal from glaucomatous eyes. Therefore, the HRT II has been used for glaucoma screening [11–13].

The Moorfields Regression Analysis (MRA) of the stereometric parameters obtained by the HRT II is a useful method of diagnosing glaucoma based on the morphological parameters of optic discs. The MRA program is based on comparing the rim area and disc area of a glaucoma suspect to the normal database embedded in the instrument [11]. From the results of the comparisons, a determination can be made on whether the eye is non-glaucomatous or glaucomatous.

However, when the size of the optic nerve head is smaller or larger than the normal size, it is difficult to diagnose glaucoma by the MRA. Based on the Tajimi study, the diagnostic power of detecting glaucoma by the MRA program is reduced when the disc size becomes larger than the normal size [14].

In addition to the MRA, several statistical methods have been proposed by Mikelberg et al., Lester et al. and Bathija et al. to differentiate normal from glaucomatous optic discs [15–17]. Ford et al. reported that these methods of analysis had similar sensitivities once their specificities were equalized. However, the diagnostic power of these methods decreases when the disc size is large, because these methods are based mainly on the data of eyes with a normal disc size [18].

The purpose of this study was to determine the stereometric parameters of eyes with large optic discs without visual field defects. The parameters were compared to those of diagnosed glaucomatous eyes with large optic discs, and we identified the disc parameters which can be used to diagnose glaucoma. We then created a new formula based on these parameters to diagnose glaucoma in eyes with a large optic disc.

Materials and Methods

Patients

Patients who were being treated at Shibata Clinic of Ophthalmology from November 2005 to July 2007 were studied. Consecutive subjects who were identified with a large optic disc

area >2.82 mm^2 by the HRT II parameters during the study period underwent visual field examinations with the Humphrey Field Analyzer (HFA) 30-2 SITA Standard program (Carl Zeiss Meditec Inc, Dublin, CA). All HRT tests were performed within six months of the visual field tests.

All participants underwent a comprehensive ophthalmic examination, including a medical and family history, best-corrected visual acuity (BCVA), slit-lamp biomicroscopy, Goldmann applanation tonometry, gonioscopy and fundus examinations. Patients were excluded if they had other eye diseases that could affect the visual field other than glaucoma, those with a BCVA of 20/33 or worse and patients with a tilted optic disc.

Ethics Statement

All the data were analyzed in the Department of Ophthalmology, Hiroshima University. The study was approved by the Ethics Committee of Hiroshima University (registration number; 957) and was conducted according to the tenets of the Declaration of Helsinki.

In some kind of epidemiological researches like this study design, the Ethics Review Board of the Hiroshima University waived the need for written informed consent from the participants. We didn't get the written or verbal consent in the medical records. However, we announced the details of this study to the participants using the poster, and have disclosed the results of the examinations and study data to all participants. The Ethics committee of the Hiroshima University had approved the study procedures.

Evaluation of Visual Fields

A diagnosis of glaucoma was made based on the visual field results obtained with HFA. The results of the HFA 30-2 SITA Standard program were examined by two glaucoma specialists (SO and YK) who were blinded to other information about the eye being examined. The evaluations were carried out on all eyes, excluding those that were unreliable (fixation loss, <20%; false-positive and false-negative, <15%). Abnormal visual field data were defined by the presence of at least one abnormal hemifield that was based on the criteria proposed by Anderson and Patella [19]. The hemifield was judged to be abnormal when the pattern deviation probability plot showed a cluster of three or more non-edge contiguous points having a sensitivity of less than 5% in the upper or lower hemifield, and in one of these with a probability of less than 1%. Glaucomatous visual field changes were diagnosed when the pattern standard deviation was less than 5%, or when the glaucoma hemifield test was abnormal.

Heidelberg Retinal Tomograph II (HRT II) Parameter Measurements

The optic disc parameters were determined from the HRT II images [11,15,20]. The fundus, including the optic disc, was photographed using the HRT after pupil dilation. The image quality of all the HRT images was checked manually by an experienced operator, and the optic disc margin (contour line) was outlined around the inner margin of the peripapillary scleral rings by the same operator (KY). The analysis was restricted to eyes that had valid optic disc measurements with the HRT II. Good image quality was defined as appropriate focus, brightness and clarity, minimal eye movements, the optic disc centered in the image and a standard deviation of the mean topographic image <40 μm. Eyes in which good-quality images could not be obtained were excluded from the analysis. The results of the MRA were evaluated by classifying borderline cases as being outside the normal limits. The HRT image recording and visual field testing were performed on the same day. All data obtained from the HRT II were analyzed (provide as supplemental data). The RNFL cross sectional area was calculated as the average distance between the retinal surface and a standard point along a contour line of the disc × the

length of contour line. The height variation contour (HVC) is the difference in retinal surface height along the contour line of the disc between the highest and lowest points. The cup shape measure represents the overall shape of the optic nerve head and has been shown to have a significant correlation with glaucomatous damage [20,21]. The cup shape measurement is independent of the reference plane and, thus, is unaffected by any variability in the reference plane [22,23]. The reference height is calculated as the average heights of the retina around the disc.

Statistical Analyses

The eyes with normal visual fields (Non-glaucoma group) and the eyes with a glaucomatous visual field (Glaucoma group) were compared based on the results of the HFA. The glaucoma group was divided into two subsets: an early glaucoma group (MD > -5 dB) and the advanced glaucoma group (MD ≤ -5dB). The correlations between the disc area and each of the HRT parameters were examined in a scatter diagram. Important HRT parameters were selected by using the stepwise method, and the odds ratio for the diagnosis of glaucoma by a logistic regression analysis was calculated. The results of the multiple logistic analyses were used to compare the results of the MRA for the global area. The optimal cut-off value of the receiver operating characteristic curve (ROC) was calculated to differentiate glaucomatous and non-glaucomatous eyes.

Comparisons of the mean values among the groups were made using *t*-tests. The JMP 9.0 Statistical Analysis System software program (SAS Institute Inc. California) was used for the calculations and statistical analyses, and a P value <0.05 was considered to be statistically significant.

Results

Participants

The demographics of the patients are summarized in Table 1. There were 225 eyes in 145 patients that were analyzed (78 eyes of 49 males and 147 eyes of 96 females). The Non-glaucomatous group included 134 eyes and the glaucoma group included 91 eyes.

Comparison of the Disc Parameters in Non-glaucomatous and Glaucomatous Eyes

The disc parameters were compared between the non-glaucomatous group and the glaucomatous group (Table 2). The disc area in the non-glaucomatous group (3.44 ± 0.50 mm^2) was not significantly different from that in the glaucomatous group (3.40 ± 0.52 mm^2). The values of the cup area, cup volume, cup-to-disc area ratio, linear cup/disc ratio, mean cup depth and the maximum cup depth of the glaucomatous group were significantly larger than those of the non-glaucomatous group. The rim area, rim volume, cup shape measure, mean RNFL thickness and RFNL cross-sectional area of the RNFL in the glaucomatous group were significantly smaller than those in the non-glaucomatous group.

Correlations between the Disc Area and the HRT Parameters

A scatter diagram shows that the cup area increased with an increase of the disc area in both the non-glaucomatous and glaucomatous groups (Fig. 1). No other HRT parameter was significantly correlated with the disc area (data not shown).

Table 1. Demographics of the study subjects.

	N	G	P*	Glaucoma			
	(n = 134)	(n = 91)		EG (n = 66)	P†	AG (n = 25)	P‡
Age (y.o)	56.70±15.91	63.59±15.20	0.001	62.55±16.50	0.017	66.36±10.85	0.004
SE (D)	−1.27±3.13	−1.60±3.27	0.456	−1.10±2.79	0.713	−2.91±4.06	0.019
MD (dB)	−0.74±1.34	−5.05±5.78	<0.001	−2.43±1.34	<0.001	−11.98±7.32	<0.001
PSD (dB)	1.79±0.88	5.71±4.35	<0.001	3.71±2.40	<0.001	10.97±3.97	<0.001

The data are expressed as the means ± SD.

N: non-glaucomatous group

G: glaucomatous group

EG: early stage glaucoma group (MD <-5dB)

AG: advanced stage glaucoma group (MD ≥-5dB)

SE: spherical equivalent

MD: mean deviation

PSD: pattern standard deviation

* Difference between the normal group and all glaucoma cases

† Difference between the normal group and the early glaucoma group

‡ Difference between the normal group and the progressive/advanced glaucoma group

doi:10.1371/journal.pone.0118920.t001

The Sensitivity and Specificity of Moorfield's Regression Analysis (MRA)

The sensitivity of the MRA was 59.0% and the specificity was 66.0% for the present patients (Table 3). The sensitivity decreased when the subjects with advanced glaucoma were excluded (Table 4). Otherwise, the sensitivity improved when the subjects in the early glaucoma group were excluded (Table 5).

The Stepwise Logistic Regression Analysis

A stepwise logistic regression analysis showed that an increase of the cup-to-disc area ratio, an increase of the height variation contour (HVC) and a decrease of the RNFL cross-sectional area were risk factors for glaucoma in eyes with a large optic disc (Table 6). The formula generated by the logistic regression analysis showed that the area under the ROC was 0.81. The sensitivity and specificity of diagnosing glaucoma were 83.5% and 68.7%, respectively, if the cut off value used for the classification was −0.69 (Fig. 2A).

The yellow line is a straight line, with an angle of 45 degrees which touches the ROC curve. a) The analysis for all subjects; b) The analysis for the non-glaucomatous and early stage glaucoma groups; c) The analysis for the non-glaucomatous and advanced stage glaucoma groups.

Before stepwise selection, there were 13 factors (disc area, cup area, cup-to-disc area ratio, rim area, height variation contour, cup volume, rim volume, mean cup depth, maximum cup depth, cup shape measure, mean RNFL thickness, RNFL cross-sectional area and reference height). The four factors shown in the table were selected using a stepwise method.

The formula generated by the logistic regression: F = −5.26 + (−1.80) x Cup volume + 9.99 x C/D area + 11.44 x HVC + (−2.461) x RNFL CS.

R^2 = 0.22, Significance of the model: $p<0.0001$

The analysis of the subjects in the Non-glaucomatous group and early glaucoma group by the logistic regression analysis with the stepwise method, in which glaucoma was the outcome variable, showed that an increase of the cup-to-disc area ratio, an increase of the HVC and a

Table 2. The HRT II parameters in the non-glaucomatous and glaucomatous eyes.

	N	G	P*	Glaucoma				
	(n = 134)	(n = 91)		EG (n = 66)	P†	AG (n = 25)	P‡	P**
Disc area (mm^2)	3.44±0.50	3.40±0.52	0.610	3.44±0.56	0.970	3.30±0.37	0.200	0.254
Rim area (mm^2)	1.96±0.43	1.57±0.43	<0.001	1.68±0.38	<0.001	1.28±0.40	<0.001	<0.001
Rim volume (mm^3)	0.45±0.19	0.32±0.17	<0.001	0.35±0.16	<0.001	0.25±0.15	<0.001	0.007
Cup area (mm^2)	1.47±0.47	1.83±0.60	<0.001	1.76±0.63	<0.001	2.02±0.46	<0.001	0.063
Cup volume (mm^3)	0.37±0.24	0.50±0.26	<0.001	0.49±0.27	0.002	0.53±0.23	0.002	0.512
C/D area	0.42±0.11	0.53±0.13	<0.001	0.51±0.12	<0.001	0.61±0.12	<0.001	<0.001
C/D linear	0.65±0.088	0.73±0.089	<0.001	0.71±0.085	<0.001	0.78±0.079	<0.001	<0.001
Mean CD (mm)	0.29±0.081	0.33±0.086	0.005	0.32±0.084	0.015	0.33±0.091	0.043	0.756
Maximum CD (mm)	0.70±0.16	0.75±0.16	0.025	0.76±0.16	0.017	0.72±0.17	0.450	0.416
CSM	−0.11±0.059	−0.085±0.062	0.001	−0.098±0.059	0.110	−0.052±0.059	<0.001	0.001
RNFLT (mm)	0.23±0.077	0.19±0.073	<0.001	0.20±0.073	0.006	0.17±0.072	<0.001	0.097
RNFL CS (mm^2)	1.48±0.51	1.23±0.50	<0.001	1.29±0.51	0.011	1.08±0.46	<0.001	0.075
HVC (mm)	0.38±0.11	0.38±0.13	0.830	0.39±0.12	0.500	0.36±0.15	0.490	0.345
RH (mm)	0.38±0.10	0.36±0.10	0.300	0.36±0.10	0.170	0.38±0.11	0.910	0.329

The data are expressed as the means ± SD.

N: non-glaucomatous group

G: glaucomatous group

EG: early stage glaucoma group (MD<-5dB)

AG: advanced stage glaucoma group (MD ≥-5dB)

C/D area: cup-to-disc area ratio

C/D linear: linear cup/disc ratio

CD: cup depth

CSM: cup shape measure

RNFLT: mean RNFL thickness

RNFL CS: RNFL cross-sectional area

HVC: height variation contour

RH: reference height

* Difference between the normal patients and all glaucoma cases

† Difference between the normal and early glaucoma groups

‡ Difference between the normal and progressive/advanced glaucoma groups

** Difference between the early glaucoma and progressive/advanced glaucoma groups

doi:10.1371/journal.pone.0118920.t002

decrease of the RNFL cross-sectional area were risk factors for early stage glaucoma (Table 7). The formula generated by the logistic regression analysis showed that the area under the ROC was 0.79. The sensitivity and specificity for diagnosing glaucoma were 92.4% and 57.5%, respectively, if the cut-off value used for the classification was −1.19 (Fig. 2B).

Before the stepwise selection, there were 13 factors (shown in Table 6). The three factors shown in the table were selected using with a stepwise method.

The formula generated by the logistic regression: F = −4.18 + 5.35 x C/D area + 12.3 x HVC + (−2.6) x RNFL CS.

C/D area: cup-to-disc area ratio; HVC: height variation contour;

RNFL CS: RNFL cross-sectional area

R^2 = 0.16, Significance of the model: $p<0.0001$

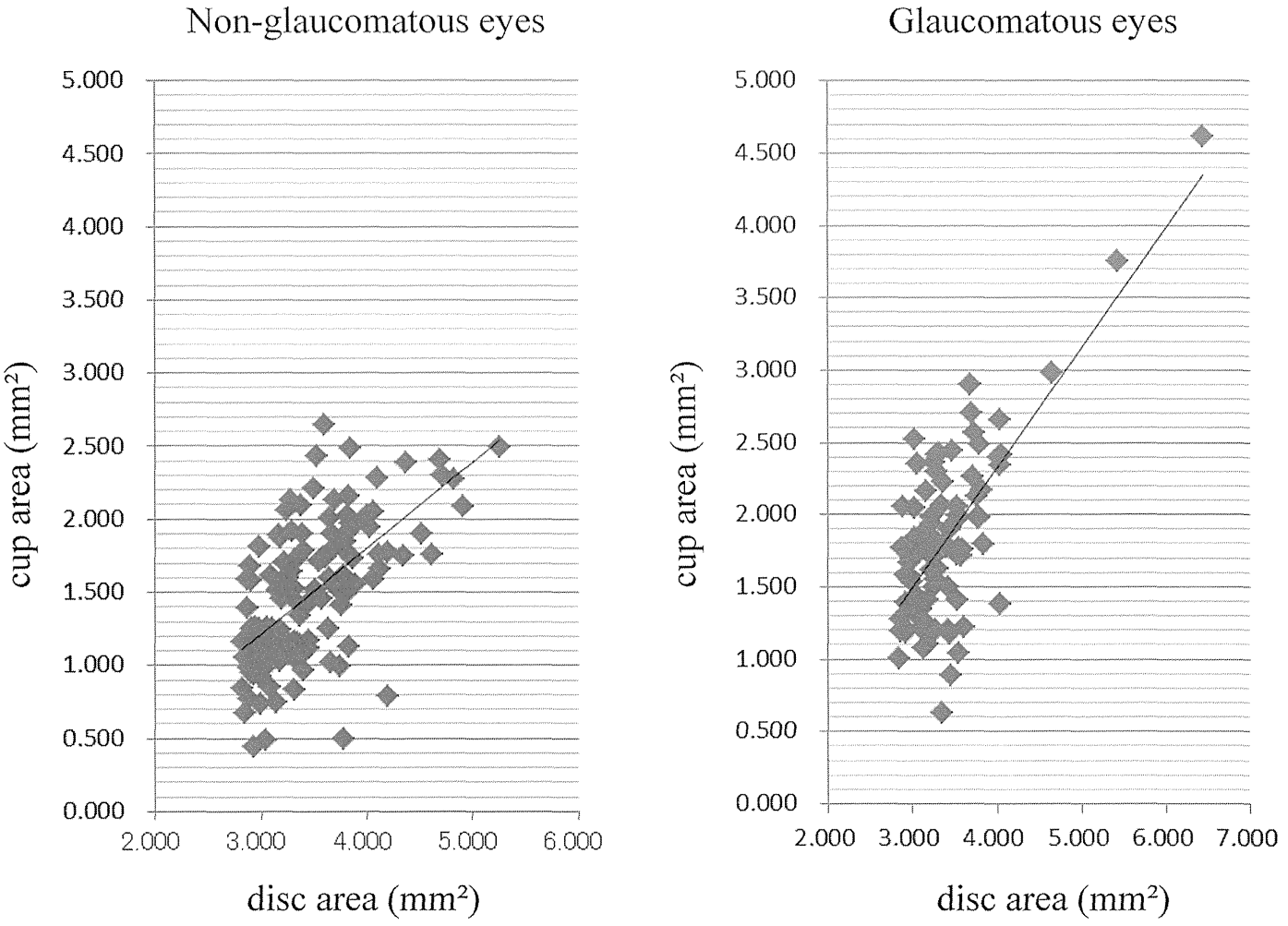

Fig 1. Scatter diagrams showing the correlations between the disc area and cup area. (Left figure) R^2 = 0.384, cup area = 0.585 x disc area—0.540. (Right figure) R^2 = 0.515, cup area = 0.825 x disc area—0.974.

doi:10.1371/journal.pone.0118920.g001

An analysis of the subjects in the non-glaucomatous group and the advanced glaucoma group by a stepwise logistic regression analysis showed that an increase in the cup-to-disc area ratio and a decrease of the cup volume were risk factors for glaucoma (Table 8). The formula

Table 3. The sensitivity and specificity of the MRA (Moorfield's Regression Analysis) for all subjects (n = 225).

	MRA	Sector						
	Classification	global	temporal	tmp/sup	tmp/inf	nasal	nsl/sup	nsl/inf
Sensitivity (%)	88	59	34	39	65	54	54	66
Specificity (%)	36	66	88	90	66	57	70	61

tmp: temporal
nsl: nasal
sup: superior
inf: inferior

doi:10.1371/journal.pone.0118920.t003

Table 4. The sensitivity and specificity of the MRA (Moorfield's Regression Analysis) for the non-glaucomatous group and the early stage glaucoma group (n = 200).

	MRA	Sector						
	Classification	global	temporal	tmp/sup	tmp/inf	nasal	nsl/sup	nsl/inf
Sensitivity (%)	86	51	25	29	59	48	48	58
Specificity (%)	36	66	88	90	66	57	70	61

tmp: temporal
nsl: nasal
sup: superior
inf: inferior

doi:10.1371/journal.pone.0118920.t004

generated by the logistic regression analysis showed that the area under the ROC was 0.91. The sensitivity and specificity for diagnosing glaucoma were 92.0% and 83.7%, respectively, if the cut-off value used for the classification was −1.94 (Fig. 2C).

Before stepwise selection, there were 13 factors (shown in Table 6). The two factors shown in the table were selected with a stepwise method.

The formula generated by the logistic regression: F = −11.66 + (−6.17) x Cup volume + 24.81 x C/D area.

C/D area: cup-to-disc area ratio

$R^2 = 0.44$, Significance of the model: $p<0.0001$

Discussion

It is difficult to recognize the morphological changes in a glaucomatous optic disc when the disc size is large because a large disc area is significantly correlated with the optic cup area in both glaucomatous and non-glaucomatous eyes. We therefore determined the morphological features of large optic discs in eyes that were diagnosed with glaucoma by HFA. We were also able to develop a new formula to diagnose glaucoma based on the stereometric parameters in eyes with large optic discs.

Table 5. The sensitivity and specificity of the MRA (Moorfield's Regression Analysis) for the non-glaucomatous group and the advanced stage glaucoma group (n = 159).

	MRA	Sector						
	Classification	global	temporal	tmp/sup	tmp/inf	nasal	nsl/sup	nsl/inf
Sensitivity (%)	96	80	60	68	80	72	72	88
Specificity (%)	36	66	88	90	66	57	70	61

tmp: temporal
nsl: nasal
sup: superior
inf: inferior

doi:10.1371/journal.pone.0118920.t005

Table 6. The results of the logistic regression analysis with a stepwise method, in which glaucoma was the outcome variable among all subjects.

Variable	Odds Ratio	95% Confidence Interval			*P*
Cup volume ($\times 10^{-1}$)	0.83	0.67	-	1.03	0.10
C/D area ($\times 10^{-1}$)	2.72	1.70	-	4.52	<.0001
HVC ($\times 10^{-1}$)	3.14	1.80	-	5.81	0.0001
RNFL CS	0.085	0.021	-	0.31	0.0003

doi:10.1371/journal.pone.0118920.t006

The Differences in the Morphological Features of Large Discs Between Glaucomatous and Non-glaucomatous Eyes

Our results showed that all of the parameters related to disc cupping, viz., the cup area, cup volume, cup-to-disc area ratio, linear cup/disc ratio, mean cup disc and maximum cup depth, were significantly larger in the eyes with glaucoma than in the eyes without glaucoma. The parameters related to the disc rim, viz., the rim area, rim volume and the circumpapillary nerve fiber layer thickness (mean RNFL thickness, RNFL cross-sectional area) in glaucomatous eyes were significantly smaller than those in eyes without glaucoma.

Similar findings were previously noted in eyes with normal-sized optic discs. For example, Medeiros reported that the rim-related parameters, including the rim area, rim volume and rim-to-disc area, of glaucomatous eyes were significantly smaller than those in eyes without glaucoma [24]. Medeiros also reported statistically significant differences in the cup parameters, viz., the cup-to-disc area ratio and the linear cup-to-disc ratio, between glaucomatous and non-glaucomatous eyes with normal-sized optic discs [24]. Uchida et al. reported that the area and volume of the optic cup were significantly larger in glaucomatous eyes than in normal eyes [20].

Our results on eyes with large optic discs showed that the maximum cup depth and mean cup depth in the early stage glaucoma group was significantly larger than those in the non-glaucomatous group (Table 2). However, the differences in these parameters between the early stage and advanced stage glaucoma groups were small, and the differences were not significant. Thus, the evaluation of whether glaucoma has progressed by using the cup depth parameters does not lead to accurate results. On the other hand, the rim area in advanced glaucomatous eyes was significantly smaller than that in the early stage glaucomatous subjects, and the cup-to-disc area ratio and linear cup/disc ratio were significantly larger in advanced stage than in early stage glaucomatous eyes. These results indicate that the cup depth reaches its maximum change at the early stage of glaucoma, but that the rim thinning continues to decrease for a longer duration in eyes with large optic discs.

Diagnosing Glaucoma by the HRT Stereometric Parameters in Eyes with Large Optic Discs

We used the stereometric parameters determined by HRT II to create a new formula for eyes with a large optic disc. We used the MRA to determine the validity of the new formula, because it is the default program included for the HRT II and is easy to use. The MRA uses the disc rim area, disc area and age for its calculations. In our study, an increase in the cup-to-disc area ratio, an increase in the HVC and a reduction of the RNFL cross-sectional area were risk factors for glaucoma. The HVC is the difference in the height between the highest retinal surface and the lowest retinal surface along the contour line. The RNFL cross-sectional area is the average distance between the retinal surface and a standard point along the contour line of the disc

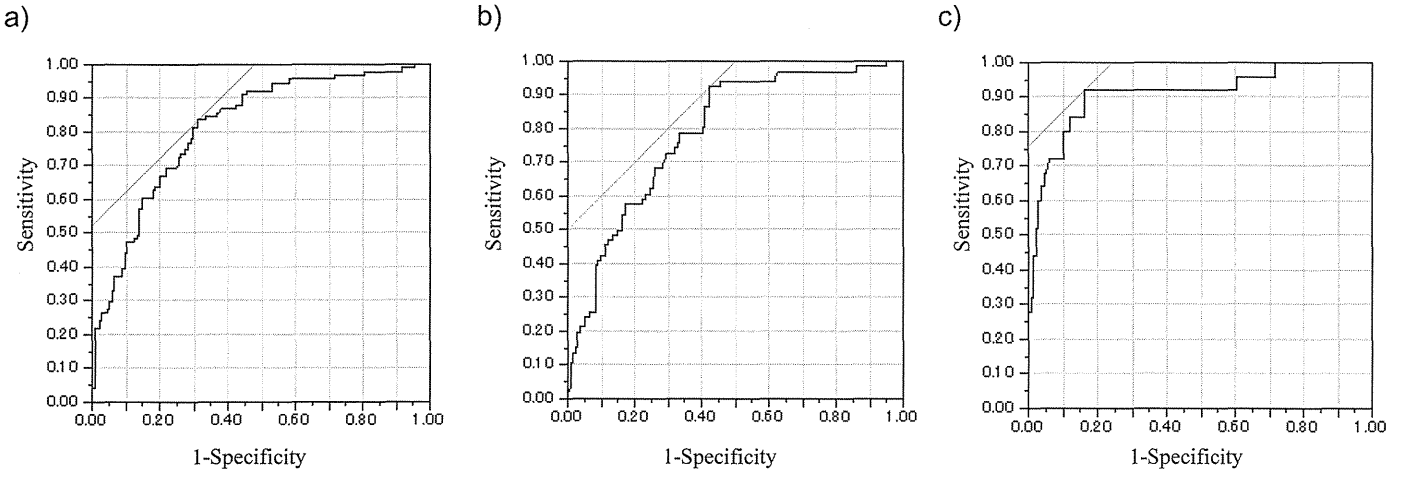

Fig 2. The ROC curves of the logistic regression analyses with the stepwise method in which glaucoma was the outcome variable among all subjects.

doi:10.1371/journal.pone.0118920.g002

x the length of contour line. Both parameters are related to the thickness of the circumpapillary retinal nerve fiber layer. An increase of the HVC and decrease of the RNFL cross-sectional area suggest glaucomatous changes, because the RNFL becomes thinner in glaucomatous eyes. The diagnostic power, which is the sum of the sensitivity and specificity, of our new formula that included the cup volume, cup-to-disc area ratio, HVC and RNFL cross-sectional area was 1.53, whereas the diagnostic power of the MRA was 1.25. The large discs are identical to normal-sized discs in terms of the RNFL thickness [10,25]. Oddone et al. showed that the diagnostic accuracy of quantitative RNFL assessments measured with Cirrus HD-OCT and GDx-VCC is high and insignificantly affected by the size of the optic disc [26]. Furthermore, they reported that it may provide more consistent diagnostic outcomes across small and large discs when compared with the optic nerve head assessment, such as the MRA program measured with HRT [26]. Therefore, it is important to evaluate the parameters related to the retinal nerve fiber thickness, which are not affected by the disc size, to diagnose glaucoma in eyes with large optic discs.

The parameters related to the RNFL thickness were not selected by a logistic regression analysis when we differentiated eyes in the advanced stage and non-glaucomatous groups. These findings are not contradictory to the study by Hood et al., who reported a good correlation between the circumpapillary RNFL thickness obtained by OCT and the visual field loss (Mean Deviation, MD) when the field loss was >-6 dB. This is because when the MD is < -6.0 dB, the RNFL changes are too small to detect the progression of glaucoma [27].

Table 7. The results of the logistic regression analysis with the stepwise method, in which glaucoma was the outcome variable between the non-glaucomatous group and the early stage glaucoma group.

Variable	Odds Ratio	95% Confidence Interval			*P*
C/D area ($\times 10^{-1}$)	1.71	1.25	-	2.38	0.001
HVC ($\times 10^{-1}$)	3.42	1.93	-	6.45	<.0001
RNFL CS	0.073	0.018	-	0.27	<.0001

doi:10.1371/journal.pone.0118920.t007

Table 8. The results of the logistic regression analysis with the stepwise method, in which glaucoma was the outcome variable between the non-glaucomatous group and the advanced stage glaucoma group.

Variable	Odds Ratio	95% Confidence Interval			*P*
Cup volume ($\times 10^{-1}$)	0.54	0.35	-	0.77	0.002
C/D area ($\times 10^{-1}$)	11.96	5.23	-	33.77	<0.001

doi:10.1371/journal.pone.0118920.t008

Another interesting result of this study was the high incidence, 40.4%, of glaucoma in eyes with a large optic disc. In the general population, the incidence of glaucoma was 5.0% in the Tajimi study and 3.5% in the Namil study [28,29]. It is difficult to draw conclusions about the prevalence of glaucoma in cases with large discs, because this was a single center case-control study. However, all subjects with a disc > 2.82mm^2 by HRT II were included in this study. This suggested that a large optic disc may be a risk factor for glaucoma. Our present findings are similar to past reports suggesting that a large optic disc is a risk factor for glaucoma [30–32].

There are a few limitations associated with our study. First, this was a single center, case-control study, and we analyzed both eyes of each patient when the subjects had large discs in both eyes. Abe et al. reported that all HRT parameters were significantly correlated between right and left eyes. However, their results suggested that subjects with larger discs tended to show greater inter-eye absolute differences in these HRT parameters [33]. In our 147 consecutive cases, 69 subjects had a large disc in one eye and 78 subjects had a large disc in both eyes. The disc features were not correlated between the right and left eyes. This is the reason why we included the data from both eyes even when both eyes had a large disc. Second, we have not confirmed the ability of our new formula to discriminate the glaucoma group from the non-glaucoma group in another set of subjects with a large optic disc area.

In conclusion, our data indicate that the cup-to-disc area ratio, HVC and RNFL cross-sectional area are significant HRT parameters that are more appropriate for diagnosing early stage glaucoma, and an increase in the cup-to-disc area ratio and a decrease of the cup volume were risk factors for advanced glaucoma in eyes with large optic discs.

Supporting Information

S1 Dataset. The patients' information, HFA, and HRT data.
(XLS)

Author Contributions

Conceived and designed the experiments: SO YK TS. Performed the experiments: SO. Analyzed the data: SO KY. Contributed reagents/materials/analysis tools: SO KY TS. Wrote the paper: SO KY.

References

1. Sommer A, Pollack I, Maumenee AE. Optic disc parameters and onset of glaucomatous field loss. II. Static screening criteria. Arch Ophthalmol. 1979; 97: 1449–1454. PMID: 464867
2. Sommer A, Katz J, Quigley HA, Miller NR, Robin AL, Richter RC, et al. Clinically detectable nerve fiber atrophy precedes the onset of glaucomatous field loss. Arch Ophthalmol. 1991; 109: 77–83. PMID: 1987954
3. Quigley HA, Miller NR, George T. Clinical evaluation of nerve fiber layer atrophy as an indicator of glaucomatous optic nerve damage. Arch Ophthalmol. 1980; 98: 1564–1571. PMID: 7425916

4. Quigley HA, Katz J, Derick RJ, Gilbert D, Sommer A. An evaluation of optic disc and nerve fiber layer examinations in monitoring progression of early glaucoma damage. Ophthalmology. 1992; 99: 19–28. PMID: 1741133
5. Quigley HA, Green WR. The histology of human glaucoma cupping and optic nerve damage: clinicopathologic correlation in 21 eyes. Ophthalmology. 1979; 86: 1803–1830. PMID: 553256
6. Pederson JE, Anderson DR. The mode of progressive disc cupping in ocular hypertension and glaucoma. Arch Ophthalmol. 1980; 98: 490–495. PMID: 7362506
7. Jonas JB, Bergua A, Schmitz-Valckenberg P, Papastathopoulos KI, Budde WM. Ranking of optic disc variables for detection of glaucomatous optic nerve damage. Invest Ophthalmol Vis Sci. 2000; 41: 1764–1773. PMID: 10845597
8. Foster PJ, Buhrmann R, Quigley HA, Johnson GJ. The definition and classification of glaucoma in prevalence surveys. Br J Ophthalmol. 2002; 86: 238–242. PMID: 11815354
9. Hoffmann EM, Zangwill LM, Crowston JG, Weinreb RN. Optic disk size and glaucoma. Surv Ophthalmol. 2007; 52: 32–49. PMID: 17212989
10. Onmez FE, Satana B, Altan C, Basarir B, Demirok A. A comparison of optic nerve head topographic measurements by Stratus OCT in patients with macrodiscs and normal-sized healthy discs. J Glaucoma. 2014; 23: e152–156. doi: 10.1097/IJG.0000000000000021 PMID: 24240877
11. Wollstein G, Garway-Heath DF, Hitchings RA. Identification of early glaucoma cases with the scanning laser ophthalmoscope. Ophthalmology. 1998; 105: 1557–1563. PMID: 9709774
12. Miglior S, Guareschi M, Albe E, Gomarasca S, Vavassori M, Orzalesi N. Detection of glaucomatous visual field changes using the Moorfields regression analysis of the Heidelberg retina tomograph. Am J Ophthalmol. 2003; 136: 26–33. PMID: 12834666
13. Miglior S, Albe E, Guareschi M, Rossetti L, Orzalesi N. Intraobserver and interobserver reproducibility in the evaluation of optic disc stereometric parameters by Heidelberg Retina Tomograph. Ophthalmology. 2002; 109: 1072–1077. PMID: 12045046
14. Saito H, Tsutsumi T, Araie M, Tomidokoro A, Iwase A. Sensitivity and specificity of the Heidelberg Retina Tomograph II Version 3.0 in a population-based study: the Tajimi Study. Ophthalmology. 2009; 116: 1854–1861. doi: 10.1016/j.ophtha.2009.03.048 PMID: 19660814
15. Mikelberg FS, Parfitt CM, Swindale NV, Graham SL, Drance SM, Gosine R. Ability of the heidelberg retina tomograph to detect early glaucomatous visual field loss. J Glaucoma. 1995; 4: 242–247. PMID: 19920681
16. Iester M, Mikelberg FS, Drance SM. The effect of optic disc size on diagnostic precision with the Heidelberg retina tomograph. Ophthalmology. 1997; 104: 545–548. PMID: 9082287
17. Bathija R, Zangwill L, Berry CC, Sample PA, Weinreb RN. Detection of early glaucomatous structural damage with confocal scanning laser tomography. J Glaucoma. 1998; 7: 121–127. PMID: 9559499
18. Ford BA, Artes PH, McCormick TA, Nicolela MT, LeBlanc RP, Chauhan BC. Comparison of data analysis tools for detection of glaucoma with the Heidelberg Retina Tomograph. Ophthalmology. 2003; 110: 1145–1150. PMID: 12799239
19. Anderson DR, Patella VM. Automated static perimetry. St. Louis: Mosby; 1999.
20. Uchida H, Brigatti L, Caprioli J. Detection of structural damage from glaucoma with confocal laser image analysis. Invest Ophthalmol Vis Sci. 1996; 37: 2393–2401. PMID: 8933756
21. Teesalu P, Vihanninjoki K, Airaksinen PJ, Tuulonen A, Laara E. Correlation of blue-on-yellow visual fields with scanning confocal laser optic disc measurements. Invest Ophthalmol Vis Sci. 1997; 38: 2452–2459. PMID: 9375562
22. Vihanninjoki K, Burk RO, Teesalu P, Tuulonen A, Airaksinen PJ. Optic disc biomorphometry with the Heidelberg Retina Tomograph at different reference levels. Acta Ophthalmol Scand. 2002; 80: 47–53. PMID: 11906304
23. Tan JC, Hitchings RA. Reference plane definition and reproducibility in optic nerve head images. Invest Ophthalmol Vis Sci. 2003; 44: 1132–1137. PMID: 12601040
24. Medeiros FA, Vizzeri G, Zangwill LM, Alencar LM, Sample PA, Weinreb RN. Comparison of retinal nerve fiber layer and optic disc imaging for diagnosing glaucoma in patients suspected of having the disease. Ophthalmology. 2008; 115: 1340–1346. doi: 10.1016/j.ophtha.2007.11.008 PMID: 18207246
25. Costa AM, Cronemberger S. Optic disc and retinal nerve fiber layer thickness descriptive analysis in megalopapilla. J Glaucoma. 2014; 23: 368–371. doi: 10.1097/IJG.0b013e318279b3af PMID: 23296371
26. Oddone F, Centofanti M, Tanga L, Parravano M, Michelessi M, Schiavone M, et al. Influence of disc size on optic nerve head versus retinal nerve fiber layer assessment for diagnosing glaucoma. Ophthalmology. 2011; 118: 1340–1347. doi: 10.1016/j.ophtha.2010.12.017 PMID: 21474186

27. Hood DC, Anderson SC, Wall M, Raza AS, Kardon RH. A test of a linear model of glaucomatous structure-function loss reveals sources of variability in retinal nerve fiber and visual field measurements. Invest Ophthalmol Vis Sci. 2009; 50: 4254–4266. doi: 10.1167/iovs.08-2697 PMID: 19443710

28. Kim CS, Seong GJ, Lee NH, Song KC. Prevalence of primary open-angle glaucoma in central South Korea the Namil study. Ophthalmology. 2011; 118: 1024–1030. doi: 10.1016/j.ophtha.2010.10.016 PMID: 21269703

29. Iwase A, Suzuki Y, Araie M, Yamamoto T, Abe H, Shirato S, et al. The prevalence of primary open-angle glaucoma in Japanese: the Tajimi Study. Ophthalmology. 2004; 111: 1641–1648. PMID: 15350316

30. Tuulonen A, Airaksinen PJ. Optic disc size in exfoliative, primary open angle, and low-tension glaucoma. Arch Ophthalmol. 1992; 110: 211–213. PMID: 1736870

31. Tomita G, Nyman K, Raitta C, Kawamura M. Interocular asymmetry of optic disc size and its relevance to visual field loss in normal-tension glaucoma. Graefes Arch Clin Exp Ophthalmol. 1994; 232: 290–296. PMID: 8045438

32. Burk RO, Rohrschneider K, Noack H, Volcker HE. Are large optic nerve heads susceptible to glaucomatous damage at normal intraocular pressure? A three-dimensional study by laser scanning tomography. Graefes Arch Clin Exp Ophthalmol. 1992; 230: 552–560. PMID: 1427140

33. Abe H, Shirakashi M, Tsutsumi T, Araie M, Tomidokoro A, Iwase A, et al. Laser scanning tomography of optic discs of the normal Japanese population in a population-based setting. Ophthalmology. 2009; 116: 223–230. doi: 10.1016/j.ophtha.2008.09.013 PMID: 19084274

Macular Choroidal Thickness and Volume in Healthy Pediatric Individuals Measured by Swept-Source Optical Coherence Tomography

Toshihiko Nagasawa,[1,2] Yoshinori Mitamura,[3] Takashi Katome,[3] Kayo Shinomiya,[3] Takeshi Naito,[3] Daisuke Nagasato,[1] Yukiko Shimizu,[1] Hitoshi Tabuchi,[1] and Yoshiaki Kiuchi[2]

[1]Department of Ophthalmology, Saneikai Tsukazaki Hospital, Himeji, Japan
[2]Department of Ophthalmology and Visual Sciences, Graduate School of Biomedical Sciences, Hiroshima University, Hiroshima, Japan
[3]Department of Ophthalmology, Institute of Health Biosciences, The University of Tokushima Graduate School, Tokushima, Japan

Correspondence: Yoshinori Mitamura, Department of Ophthalmology, Institute of Health Biosciences, The University of Tokushima Graduate School, 3-18-15 Kuramoto, Tokushima 770-8503, Japan; ymita@tokushima-u.ac.jp.

Submitted: May 3, 2013
Accepted: September 22, 2013

Citation: Nagasawa T, Mitamura Y, Katome T, et al. Macular choroidal thickness and volume in healthy pediatric individuals measured by swept-source optical coherence tomography. *Invest Ophthalmol Vis Sci.* 2013;54:7068–7074. DOI:10.1167/iovs.13-12350

Purpose. We evaluated the choroidal thickness and volume in healthy pediatric individuals by swept-source optical coherence tomography (SS-OCT) and compared the findings to those of adults.

Methods. We examined 100 eyes of 100 healthy pediatric volunteers (3–15 years) and 83 eyes of 83 healthy adult volunteers (24–87 years) by SS-OCT with a tunable long wavelength laser source. The three-dimensional raster scan protocol was used to construct a choroidal thickness map. When the built-in software delineated an erroneous choroscleral border in the B-scan images, manual segmentation was used.

Results. The central choroidal thickness and volume within a 1.0-mm circle were significantly larger in the children (260.4 ± 57.2 μm, 0.205 ± 0.045 mm^3) than in the adults (206.1 ± 72.5 μm, 0.160 ± 0.056 mm^3, both $P < 0.0001$). In the children, the mean choroidal thickness of the nasal area was significantly thinner than that of all other areas ($P < 0.005$). Pediatric choroidal thinning with increasing age in the central area was faster than that in the outer areas. Stepwise regression analysis showed that the axial length and body mass index had the highest correlation with the choroidal thickness ($R^2 = 0.313$, $P < 0.0001$).

Conclusions. The macular choroidal thickness and volume in the pediatric individuals were significantly larger than those in the adults. The pediatric choroidal thinning with increasing age is more rapid in the central area. Pediatric choroidal thickness is associated with several systemic or ocular parameters, especially the axial length and body mass index. These differences should be remembered when the choroidal thickness is evaluated in pediatric patients with retinochoroidal diseases.

Keywords: swept-source optical coherence tomography, choroidal thickness, choroidal volume, pediatric individual, adult

Enhanced depth imaging (EDI) optical coherence tomography (OCT) based on spectral-domain OCT (SD-OCT) technology has allowed clinicians to examine the choroidal thickness in healthy eyes and eyes with various pathologies.[1–6]

Swept-source OCT (SS-OCT) uses a swept wavelength laser as the light source,[7,8] and a recently developed SS-OCT instrument has an A-scan repetition rate of 100,000 Hz. When the coherence length of the source is appropriate, SS-OCT can achieve much less roll-off in sensitivity with increasing depth than with the standard SD-OCT.[9] In addition, the current SS-OCT instrument uses a longer center wavelength, which improved its ability to penetrate deeply into tissues.

With this SS-OCT instrument, precise evaluations of deeper structures of the eye, such as the choroid and retrobulbar optic nerve, are possible.[10] Ikuno et al.[11] studied the choroidal thickness of healthy adult subjects with an SS-OCT. Because the current SS-OCT instrument has a high scan rate and a relatively low sensitivity roll-off versus depth, a three-dimensional (3D) high contrast image of the choroid can be obtained.[12–14] Recently, Hirata et al.[15] constructed a choroidal thickness map using the 3D raster scan protocol of the SS-OCT, and they investigated the macular choroidal thickness and volume of healthy adults.

The choroidal thickness determined by EDI-OCT or SS-OCT has been reported to decrease with age in healthy adult eyes.[3,11,15–18] However, information on the choroidal thickness in children remains limited.[19–21] In these studies, the choroidal thickness of only a few sampling points[19,20] or the average choroidal thickness on the scan line[21] was examined. Thus, the exact choroidal thickness could not be determined, because the thickness can be affected by focal changes,[22,23] and by irregularities of the choroscleral border.[5] In addition, the location of the choroscleral border was done manually. It would be better to construct a map of the choroid with the borders selected objectively to overcome these limitations.

Thus, the purpose of this study was to determine the choroidal thickness and volume by constructing choroidal thickness maps in a pediatric population. To accomplish this,

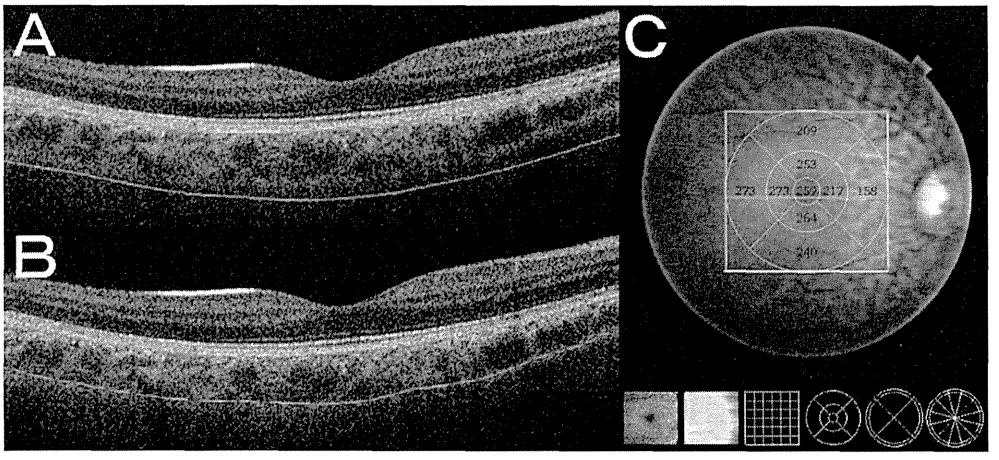

FIGURE 1. Choroidal thickness map of a healthy 7-year-old boy obtained by SS-OCT. The 3D raster scan protocol with 512 A-scans × 256 B-scans was used to obtain 3D imaging data of the 6 × 6-mm area. (**A**) Erroneous placement of the chorioscleral border made by the automatic built-in software in one of the B-scan images of the 3D data set. Although the tracing of the retinal pigment epithelium is correct, that of the chorioscleral border is not accurate. (**B**) Manual segmentation of the chorioscleral border in the same B-scan image. Only when the built-in software delineated an erroneous chorioscleral border, manual segmentation was performed. (**C**) By analyzing the B-scan images of the 3D data set, a choroidal thickness map of the 6 × 6-mm area centered on the fovea was created. By applying the ETDRS grid to the map, the mean choroidal thickness was obtained for each sector.

we scanned the macular area of healthy pediatric eyes using the 3D raster scan protocol, and constructed a choroidal thickness map. By using the Early Treatment Diabetic Retinopathy Study (ETDRS)[24] grid for the choroidal thickness maps, we were able to determine the mean choroidal thickness and volume in each sector of the grid. The findings obtained from the pediatric individuals were compared to those obtained from adults.

SUBJECTS AND METHODS

We studied 100 eyes of 100 healthy pediatric volunteers, with a mean ± SD age of 7.9 ± 3.1 years and a range from 3 to 15 years (45 boys and 55 girls), and 83 eyes of 83 healthy adult volunteers, with a mean age of 54.5 ± 19.3 years and a range from 24 to 87 years (43 men and 40 women) at Saneikai Tsukazaki Hospital and Tokushima University Hospital. All subjects had no ophthalmic or systemic signs or symptoms. One eye was chosen randomly for the statistical analyses. The procedures used conformed to the tenets of the Declaration of Helsinki, and an informed consent was obtained from either the subjects or their legal guardians after explanation of the nature and possible consequences of the study. An approval was obtained from the Institutional Review Board of Saneikai Tsukazaki Hospital and Tokushima University Hospital to perform this study.

All subjects underwent standard ophthalmologic examinations, including measurements of the best-corrected visual acuity (BCVA), applanation tonometry, slit-lamp biomicroscopy, indirect ophthalmoscopy, autorefractometry (ARK1; Nidek, Gamagori, Japan), and axial length measurements with the IOLMaster (Carl Zeiss Meditec, Jena, Germany). All of the examinations were performed on the same day. The BCVA was measured with a standard Japanese Landolt visual acuity chart. All of the healthy pediatric volunteers had a BCVA that ranged from 0.6 to 1.5, and all adults had a BCVA that ranged from 0.9 to 1.5. The body height and weight were recorded, and the body mass index was calculated for each subject. The exclusion criteria included history of intraocular surgery; history or evidence of chorioretinal or vitreoretinal diseases, such as central serous chorioretinopathy; refractive errors (spherical equivalent) greater than ±6 diopters (D); and evidence of glaucoma. Subjects with systemic disease that might affect the choroidal thickness, such as diabetes mellitus, also were excluded.

Swept-source Optical Coherence Tomography

The macular area of the eyes was examined with the SS-OCT instrument (DRI OCT-1; Topcon, Tokyo, Japan), which was government approved for use in Japan. The light source of this SS-OCT system is a wavelength tunable laser centered at 1050 nm with an approximate 100-nm tuning range. The tissue imaging depth was 2.6 mm.

After pupillary dilation, the SS-OCT examinations were performed by trained examiners. The 3D volumetric raster scan protocol was used, and 3D volumetric data were acquired in 0.8 seconds. Each 3D scan covered an area of 6 × 6 mm centered on the fovea with 512 A-scans × 256 B-scans. To improve the image quality, 4 consecutive B-scan images of the same area were averaged. Because of the infrared scanning light, eye movements during the scans were minimized. All examinations were performed from 2:00 PM to 5:00 PM to reduce the effects of diurnal variations.[25,26]

Choroidal Thickness and Volume Measurement

From a series of 64 B-scan OCT images, each of which was created by averaging 4 consecutive B-scans, a choroidal thickness map of a 6 × 6 mm area was created by semiautomatic segmentation. Using the built-in software, the choroidal thickness was measured as the distance between the outer border of the RPE and the inner surface of the chorioscleral border. In the analyses of the 64 B-scan images, each scanned OCT image was examined to be certain that a proper tracing of the chorioscleral border had been made. When the built-in software delineated an inaccurate chorioscleral border (Fig. 1A), a manual segmentation was made by trained observers in a masked fashion (Fig. 1B).

The ETDRS grid was used for the choroidal thickness map (Fig. 1C), and the mean regional thicknesses were calculated for the nine sectors of the grid.[15,27] The inner and outer rings had diameters of 1 to 3 and 3 to 6 mm, respectively, and they were divided into superior, inferior, temporal, and nasal

Investigative Ophthalmology & Visual Science